Article

Quantifying Effects of Active Site Proximity on Rates of Methanol Dehydration to Dimethyl Ether over Chabazite Zeolites through Microkinetic Modeling

Grant Marsden, Pavlo Kostetskyy, Ryoh-Suke Sekiya, Alexander Hoffman, Songhyun Lee, Rajamani Gounder, David Hibbitts, and Linda J. Broadbelt*

Read Online

ACCESS | 📊 Metrics & More | 📰 Article Recommendations | SI Supporting Information

ABSTRACT: Control of the spatial proximity of Brønsted acid sites within the zeolite framework can result in materials with properties that are distinct from materials synthesized through conventional crystallization methods or available from commercial sources. Recent experimental evidence has shown that turnover rates of different acid-catalyzed reactions increase with the fraction of proximal sites in chabazite (CHA) zeolites. The catalytic conversion of oxygenates is an important research area, and the dehydration of methanol to dimethyl ether (DME) is a well-studied reaction as part of methanol-to-olefin chemistry catalyzed by solid acids. Published experimental data have shown that DME formation rates (per acid site) increase systematically with the fraction of proximal acid sites in the six-membered ring of CHA.

Here, we probe the effect of acid site proximity in CHA on methanol dehydration rates using electronic structure calculations and microkinetic modeling to identify the primary causes of this chemistry and their relationship to the local structure of the catalyst at the nanoscale. We report a density functional theory-parametrized microkinetic model of methanol dehydration to DME, catalyzed by acidic CHA zeolite with direct comparison to experimental data. Effects of proximal acid sites on reaction rates were captured quantitatively for a range of operating conditions and catalyst compositions, with a focus on total paired acid site concentration and reactant clustering to form higher nuclearity complexes. Next-nearest neighbor paired acid sites were identified as promoting the formation of methanol trimer clusters rather than the inhibiting tetramer or pentamer clusters, resulting in large increases in the rate for DME production due to the lower energy barriers present in the concerted methanol trimer reaction pathway. The model framework developed in this study can be extended to other zeolite materials and reaction chemistries toward the goal of rational design and development of next-generation catalytic materials and chemical processes.

KEYWORDS: active site proximity, chabazite, methanol dehydration, microkinetic modeling, density functional theory, degree of rate control, aluminum distribution, reaction flux
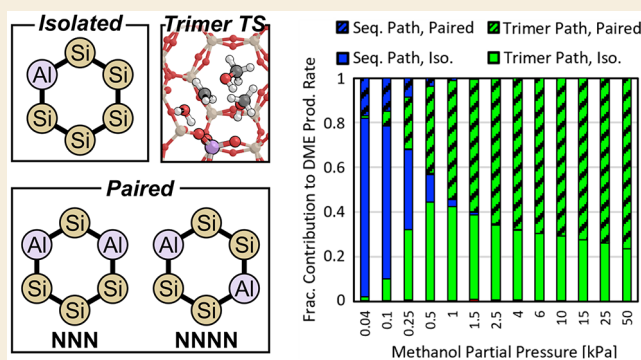
1. INTRODUCTION

Zeolites are a class of crystalline aluminosilicates with ordered micropore structures that remain stable over a range of experimental conditions and behave as catalysts for a variety of chemistries.[1,2] Since the inception of the field, significant effort has been dedicated toward tailoring the zeolite structure, pore topology, composition, and active site identity to optimize their catalytic performance.[3] Brønsted acidic (BA) zeolites are important catalysts for a range of industrial applications, frequently used for dehydration, condensation, oligomerization, catalytic cracking, and hydrocracking.[4,29]

Recent developments in experimental synthesis methods have allowed for the control of framework Al^{3+} distribution and arrangement through the use of structure-directing agents (SDAs) during hydrothermal crystallization.[5–12,15] Gounder

and co-workers[8,9,13] have reported synthetic methods to systematically control the distribution of isolated and paired framework aluminum atoms in the six-membered rings (6-MRs) of SSZ-13 [chabazite (CHA) framework] through the use of organic and inorganic SDAs of varying charge density. Other routes to influence Al distribution in CHA have also been reported, such as using nonconventional inorganic cations such as strontium and altering crystallization times
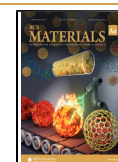
and conditions.[14,15] These synthetic advances allow controlling of the concentration and distribution of BA sites within the pore systems of zeolites, with the unique ability to tune the spatial proximity of BA sites at the nanoscale. Although framework Al−O−Al arrangements are prohibited according to Löwenstein's rule,[16] Al substitution in second-nearest-neighbor positions and at greater relative distances can occur. This control of acid site proximity can enable the tuning of the catalytic activity in known chemistries[8,9,17−20] or enabling hitherto inaccessible chemical pathways by alternate mechanisms, in which two acid sites are involved in the adsorption, activation, and stabilization of reactants, intermediates, and transition states. Recent work on methanol (MeOH) dehydration to dimethyl ether (DME) over the CHA framework has shown that the potential energy landscapes of two competing mechanisms at one BA site can be altered to a significant degree in the presence of a proximate BA site, leading to increases in turnover rates (per H$^+$).[9,20−22]

The CHA framework has a single crystallographically unique lattice tetrahedral-site (T-site) and a three-dimensional small-pore structure that imposes spatial constraints limiting the diameter of a sphere that can diffuse along its channels to 3.7 Å.[25] While the location of acid sites within zeolite frameworks remains an impactful focus of research,[12,24] the single unique T-site of CHA allows for the decoupling of the effects of location and proximity, enabling a study focused on acid site proximity and paired site configurations. Density functional theory (DFT) has been used to show that paired site configurations are stronger acids than isolated sites in CHA as calculated by deprotonation energy, the energy to remove a proton from a BA site to a noninteracting distance.[20,25] The increase in acid strength is caused by the stabilization of conjugate base anions (formed upon deprotonation) by hydrogen-bonding (H-bonding) with the other BA site when BA site pairs share a 6-MR within CHA.[20,25]

Dehydration of MeOH to DME is an industrially relevant chemical reaction that has been postulated as one of the reaction events in methanol-to-olefin chemistry and is useful in fundamental studies as a catalytic probe of acid strength and confinement effects in solid acid catalysts.[26,27] Importantly, at high reactant partial pressures, complexes of multiple alcohol molecules can form at the BA site and affect the corresponding reaction energetics by affecting the relative stabilities of intermediate and transition states along the reaction coordinate.[18,28] Additionally, turnover rates of DME formation (per H$^+$) increase with additional paired BA site motifs in the zeolite pore structure.[9] The presence of paired acid sites results in energetically favorable configurations that decrease the Gibbs free energy barriers of rate-determining steps relative to the unpaired analogues.[20]

In this work, we report a combination of experimental kinetic data, electronic structure calculations, and microkinetic modeling toward elucidating the chemistry of methanol dehydration over CHA zeolite catalysts that contain varying concentrations of paired BA sites. The effect of the presence of paired site motifs on reaction rates was quantified using DFT and shown to agree with experiments for a range of partial pressures and fractions of paired BA sites. Rigorous analysis was performed to evaluate sensitivity to the different model parameters for a range of conditions. The findings reported in this work and the modeling framework developed can be used as a basis for the analysis of different catalyst formulations,

operating conditions, and even different chemistries, demonstrating the effectiveness of multiscale modeling.

2. COMPUTATIONAL METHODS

2.1. Density Functional Theory

Fully periodic DFT calculations were performed with the Vienna ab initio software package (VASP)[29,30] implemented in the computational catalysis interface.[31] Planewave functions were constructed with the projector augmented wave method and an energy cutoff of 400 eV.[34,35] The Brillouin zone was sampled at the Γ-point for all calculations. The Perdew, Burke, and Ernzerhof (PBE) form of the generalized gradient approximation functional was used for all calculations.[32,33] Dispersion interactions were quantified by including the DFT-D3 empirical correction with Becke and Johnson damping (D3BJ).[34,35] Geometries were optimized in two steps with the goal of maximizing chemical accuracy with good computational efficiency. Structures were optimized in the first step with a conjugate gradient algorithm (IBRION = 2) using a wavefunction convergence criteria keeping energy variations between self-consistent field iterations <10^{-4} eV, and forces were computed with a fast Fourier transform grid of 1.5 times the default energy cutoff (PREC = ACCURATE in VASP). Structures were relaxed until the maximum force on any atom was <0.05 eV/Å. The same structures were reoptimized with the same conjugate gradient algorithm with wavefunctions converged to <10^{-6} eV and maximum force on any atom to <0.05 eV/Å and an FFT grid twice the planewave cutoff.

Gas-phase species were modeled in an 18 × 18 × 18 Å^3 cubic unit cell. The CHA structure was obtained from the database of the International Zeolite Association (IZA)[23] with unit cell parameters of $a = b = 13.625$ Å, $c = 14.767$ Å, $\alpha = \beta = 90.0°$, and $\gamma = 120.0°$. Some zeolite models from the IZA restructure absent simulated annealing or unit cell optimization, but this CHA model is stable without such additional treatments.[36] One to two Al were substituted in the CHA unit cell (Si/Al = 17−35); two Al pairs were placed at next-nearest neighbor (NNN) and next-NNN (NNNN) positions in the 6-MR of CHA, similar to prior work (Figure 1).[20] ^{29}Si NMR spectra of the
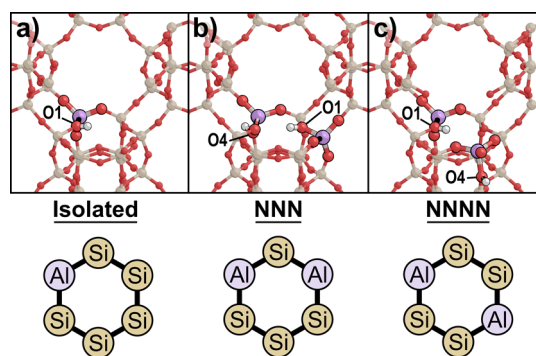
Figure 1. Different Al arrangements considered in DFT calculations in this work: (a) isolated sites, (b) NNN configurations, and (c) NNNN configurations. Top images in each panel show the most stable proton-form for the given Al arrangement.

experimental CHA samples used in this study, reported in prior work,[8] indicated that the numbers of two Al sites in NNN configurations were negligible. Adsorbates were evaluated while interacting with all four O atoms around each Al to find the preferred configuration of guest species within the framework for a given Al arrangement. The orientation of CH$_3$ moieties on methanol molecules within clusters were systematically rotated in 30° increments around the O−H axis of the O to which they were bound (i.e., the C−O−H−Al torsional angle, where the Al is an arbitrary reference), and nonsensical structures—where atoms were too close to the zeolite framework or other methanol molecules—were discarded. These reorientations preserve strong interactions

between nearby methanol molecules and generate new structures that were subsequently optimized again using the same VASP settings as above. Similar reorientation schemes were shown to reduce calculated energies by up to 60 kJ mol^{-1} for adsorbates in zeolites.[20,37] Similar sampling of the potential energy surface can be done using *ab initio* molecular dynamics (AIMD) simulations and metadynamics, from which the dynamic behavior of clusters can be determined and from which a subset of configurations can be optimized to test new structures. Similar approaches have been used previously to study alcohol and water clusters in zeolites;[28,38−42] however, such methods are computationally costly and do not necessarily perform better than simple optimization calculations when parameterizing microkinetic models.

Vibrational frequencies were used to determine zero-point vibrational energies and vibrational, rotational, and translational enthalpies (H) and free energies (G). Frequencies were computed using a fixed displacement method ($n = 2$) for all gas-phase and adsorbed species. Only guest species, protons, and AlO_4 tetrahedra were permitted to vibrate for frequency calculations in the zeolite, while the remainder of the Si and O atoms were frozen in place (a partial Hessian approach). Frequencies were used to calculate H

$$H = E_0 + \text{ZPVE} + H_{\text{vib}} + H_{\text{trans}} + H_{\text{rot}} \tag{1}$$

and G

$$G = E_0 + \text{ZPVE} + G_{\text{vib}} + G_{\text{trans}} + G_{\text{rot}} \tag{2}$$

at 415 K and 1 bar CH_3OH from statistical mechanics formalisms (see Section S.3 in the Supporting Information for details).[43] All motions from frequencies in zeolites were modeled as vibrations, including frustrated translation and rotation (i.e., their translational and rotational free energies and enthalpies were zero). Because low-frequency modes contribute disproportionately to entropy (S) estimations, calculated frequencies <60 cm^{-1} were replaced with 60 cm^{-1}, similar to our prior work.[18,20,44,45]

2.2. Microkinetic Modeling

To set up the microkinetic model, a set of ordinary differential equations describing the change in concentration of each gas and surface species was formulated. First, the rate of each of the 36 elementary steps on isolated sites was defined as

$$r_{i,\text{isolated}} = A_i \exp\left(\frac{-E_{\text{a},i}}{RT}\right) \prod_{j}^{\text{reactants}} C_j \tag{3}$$

where r_i is the rate of the ith elementary step, A_i is the pre-exponential factor, $E_{\text{a},i}$ is the activation energy, and C_j is the partial pressure of a reactant gas species or the fractional coverage of a reactant surface species. Paired active sites within the model were treated as a separate class of site on which an alternative set of kinetic and thermodynamic parameters could be accommodated based on the catalysts studied experimentally (see below). The rate of each of the 36 elementary steps on paired acid sites included an additional factor to enable using the number of isolated active sites as the integration variable, with the pathways on paired sites contributing according to their fraction of the total number of active sites, leading to

$$r_{i,\text{paired}} = \frac{\frac{n_{\text{paired}}}{n_{\text{total}}}}{1 - \frac{n_{\text{paired}}}{n_{\text{total}}}} A_i \exp\left(\frac{-E_{\text{a},i}}{RT}\right) \prod_{j}^{\text{reactants}} C_j \tag{4}$$

where n_{paired} is the number of paired acid sites, n_{total} is the number of total acid sites, and the ratio of $n_{\text{paired}}/n_{\text{total}}$ is known. From these rates, 33 ordinary differential equations covering the different gas and surface species were constructed of the form

$$\frac{dC_i}{dn_{\text{isolated}}} = \sum_{j} \nu_{i,j} r_j \tag{5}$$

where $\nu_{i,j}$ is the stoichiometric number of species i in elementary step j and n_{isolated} is the number of isolated active sites in the system. Here,

the integration variable is the number of isolated active sites in the system, determined as

$$n_{\text{isolated}} = n_{\text{total}}\left(1 - \frac{n_{\text{paired}}}{n_{\text{total}}}\right) \tag{6}$$

This set of ordinary differential equations was paired with two algebraic equations for surface species balances and combined with the design equation of a plug flow reactor (PFR) to reflect the experimental conditions. The total rate of DME formation was calculated at the outlet, where differential conversion ($<2\%$) was confirmed. The experimental reactor[9] was loaded with 0.005−0.025 g of catalyst with a silicon-to-aluminum ratio of 14−16, leading to a range of possible number of active sites from 3.8×10^{18} to 2.3×10^{19}. Thus, simulations were run with a total of 10^{19} active sites. Additionally, to match with experimental gaseous flow rates, the total molar flow rate of the inlet was set to 0.615 mol/s. Simulations were performed at a temperature of 415 K to match with the average experimental temperature. The methanol pressure was varied over a range from 35 to 52,092 Pa at specific values dictated by the experimental studies.[9]

Surface coverage of isolated and paired sites was evaluated at the outlet of the reactor, determined by the proper isolated site basis. Net rates of individual reaction pathways were determined by evaluating the net rate of each final independent reaction of each branch of the mechanism before feeding into final DME desorption. For example, the net contribution of the trimer pathway to DME production was considered to be the net rate of the iso,meoh,des,trim step. To account for uncertainty inherent within the DFT calculations due to the level of theory used in calculations of entropy and electronic structure, DFT activation energies for sensitive parameters were tuned within the bounds of ± 6 kJ/mol. In the case where a reaction was assumed to be unactivated, the pre-exponential factor was instead tuned within the bounds of 1 order of magnitude. The impact of each parameter on the overall DME formation rate for each paired percentage was determined through lowering and raising activation energies or pre-exponential factors within the previously mentioned bounds. The most impactful parameters were marked to be tuned, being selective to avoid introducing issues surrounding degrees of freedom. For the case of completely isolated sites, the marked isolated parameters were optimized through nonlinear least squares regression within the discussed bounds using the experimental data as objective points. Once a set of tuned isolated parameters was collected, these parameters were then locked, and the cases of different percentages of paired sites were analyzed equivalently. Three independent runs were performed for the three paired site percentage cases; the weighted average of these runs was taken to evaluate a single and consistent final set of parameters.

3. RESULTS AND DISCUSSION

3.1. Reaction Mechanism

Reaction mechanisms for Brønsted acid-catalyzed methanol dehydration to DME have been proposed by Iglesia and coworkers.[26,46] The authors proposed two competing pathways after an initial step of the adsorption of one methanol species on a BA site. Formation of DME can proceed through a sequential (or dissociative) pathway, in which a surface methoxy group is formed through rearrangement and dehydration of the methanol monomer. This dehydration is followed by the adsorption of another methanol molecule near a surface methoxy species, which react to form DME that desorbs into the fluid phase. Alternatively, the bound surface methanol species can follow a concerted (or associative) pathway initiated by the coordination of additional methanol molecules, forming an adsorbed dimer, that can rearrange and dehydrate. Recent work[18,47] has shown that these concerted bimolecular transition states can also form from larger

Scheme 1. Mechanism for Methanol Dehydration as Shown on Isolated Sites[a]
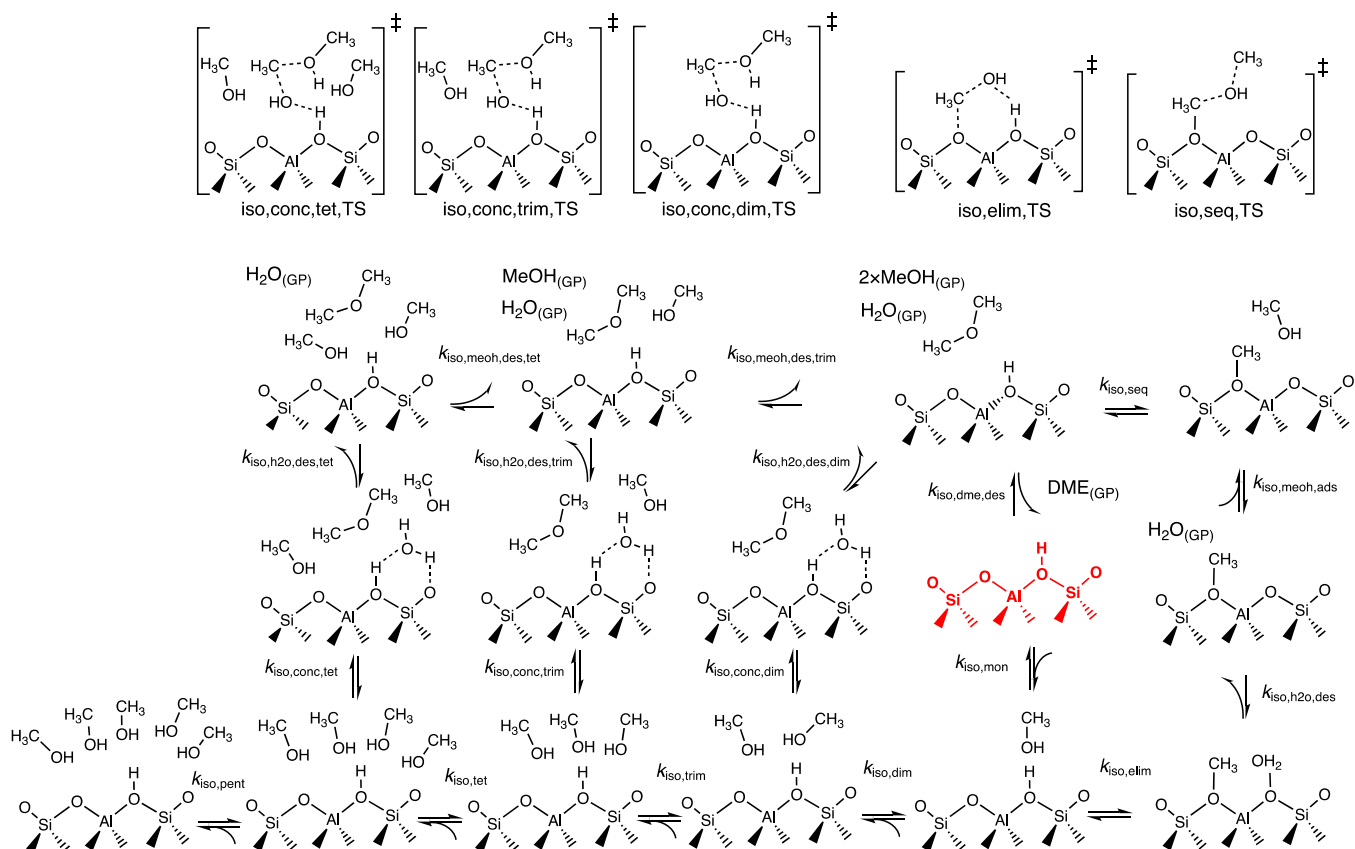
[a]Beginning with methanol adsorption ($k_{iso,mon}$), the reaction can advance through elimination to form a methoxy species ($k_{iso,elim}$) or through the adsorption of additional methanol species to form methanol dimers, trimers, tetramers, and inhibiting pentamers ($k_{iso,dim}$, $k_{iso,trim}$, $k_{iso,tet}$, and $k_{iso,pent}$, respectively) toward the concerted pathway ($k_{iso,conc}$). The reaction sequence is initiated by reactant adsorption on an unoccupied Brønsted acid site, depicted in red. Individual rate constants are specified for each elementary step and adsorption/desorption events are identified with curved reaction arrows. Gas-phase species formed upon desorption are denoted with (GP). Graphical representations of relevant transition states for the concerted and sequential pathways are shown as figure insets.

Scheme 2. Elementary Steps of Modeled Methanol Dehydration Pathways[a]

Elementary Step	Rate constant
MeOH + * ↔ MeOH*	k_{mon}
MeOH* + MeOH ↔ 2MeOH*	k_{dim}
2MeOH* ↔ DME-H$_2$O*	$k_{conc,dim}$
DME-H$_2$O* ↔ DME* + H$_2$O	$k_{h2o,des,dim}$
DME* ↔ DME + *	$k_{dme,dim}$
2MeOH* + MeOH ↔ 3MeOH*	k_{trim}
3MeOH* ↔ MeOH-DME-H$_2$O*	$k_{conc,trim}$
MeOH-DME-H$_2$O* ↔ MeOH-DME* + H$_2$O	$k_{h2o,des,trim}$
MeOH-DME* ↔ DME* + MeOH	$k_{meoh,des,trim}$
3MeOH* + MeOH ↔ 4MeOH*	k_{tet}
4MeOH* ↔ 2MeOH-DME-H$_2$O*	$k_{conc,tet}$
2MeOH-DME-H$_2$O* ↔ 2MeOH-DME* + H$_2$O	$k_{h2o,des,tet}$
2MeOH-DME* ↔ MeOH-DME* + MeOH	$k_{meoh,des,tet}$
4MeOH* + MeOH ↔ 5MeOH*	k_{pent}
MeOH* ↔ H$_2$O-CH$_3$[†] *(Rearranging H from zeolite site)*	k_{elim}
H$_2$O-CH$_3$[†] ↔ CH$_3$[†] + H$_2$O	$k_{h2o,des}$
CH$_3$[†] + MeOH ↔ MeOH-CH$_3$[†]	$k_{meoh,ads}$
MeOH-CH$_3$[†] ↔ DME* *(Reforming the H from zeolite site)*	k_{seq}

[a]An asterisk (*) indicates a surface site, whereas a dagger (†) represents a species bound to the oxygen framework of the zeolite.

methanol clusters, including trimers and tetramers, which can readily form at methanol pressures relevant to experimental studies (>10 kPa). While larger clusters were examined (up to 12 methanol molecules), the differential adsorption free energies calculated in that prior work suggest that larger

complexes are less favorable. Thus, in this work, pentamers are assumed to be nonreactive in our scheme, functioning as an inhibiting state. Methanol clusters of 2−4 methanol molecules can rearrange and dehydrate, via an S$_N$2-like transition state, to form bound DME with spectator water and methanol
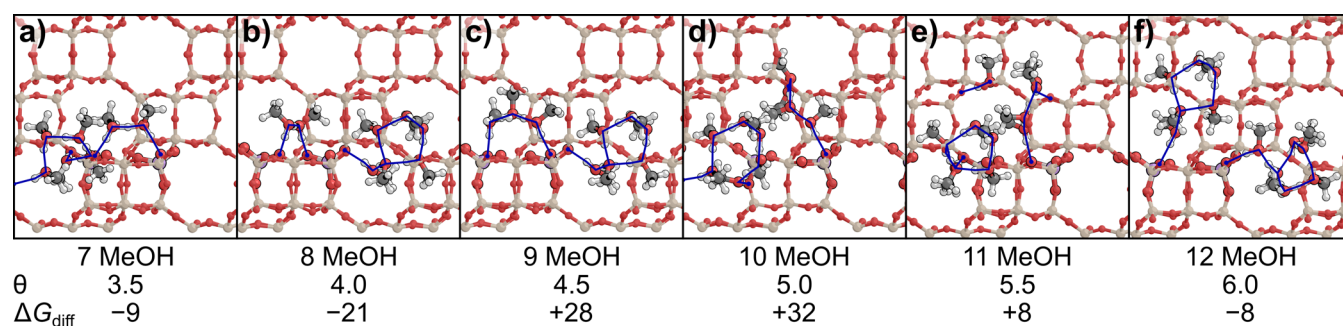
Figure 2. Structures for the most favorable configuration found for clusters of 7−12 MeOH on the NNNN pair. MeOH coverages per H$^+$ (θ) and differential binding free energies (ΔG_{diff}) in kJ mol^{-1} at 415 K are shown beneath each associated structure. Blue lines represent H-bonding networks that adsorbed MeOHs form.

molecules, which ultimately uncoordinate to form a final bound DME species that can then unbind to form gas-phase DME, thus completing the catalytic cycle. All reactions were assumed reversible and assumed to be accessible to both isolated and paired active sites. As shown in previous studies,[20] the presence of spectator methanol species resulted in increased energy barriers for the (rate-determining) elementary steps in the sequential pathway, with reported free energy barriers of 134, 155, and 143 kJ/mol in the presence of one, two, and three spectator species, respectively. Contrary to the concerted pathway, the sequential reaction barriers in the presence of spectator species were significantly less accessible, not exhibiting the promoting behavior observed in concerted reactions. Therefore, the additional elementary steps corresponding to sequential reactions in the presence of spectator methanol molecules were excluded from the reaction network in the interest of decreasing model stiffness.

Based on the mechanism described in Schemes 1 and 2 as well as the DFT results, a microkinetic model was developed to calculate DME formation rates at experimental conditions for a range of site combinations. Paired sites are modeled here with an independent set of rate constants from isolated sites, but through an identical network of chemical reactions. Thus, paired sites are not treated using a two-site kinetic model, but the effects of pairing are captured by differences between k_{iso} and k_{pair} rate constants. In microkinetic modeling, no assumptions about the rate-determining step(s) are made, and instead, the rates of a complete set of plausible elementary steps are formulated according to mass action kinetics. The results of the model solution are then analyzed to identify major pathways that carry the flux, surface species coverage, and product distribution. As implemented here, the results of the microkinetic model were queried to probe the prevalence of the concerted and sequential pathways for a wide range of operating conditions at each site type, and within the possible routes comprising the concerted pathway which methanol cluster size gave the highest contribution to the overall rate. In addition, the relative rates of individual steps on isolated and paired sites could be directly quantified.

3.2. DFT Calculations

Polar molecules can form clusters around Brønsted acid sites or polar defects within zeolite frameworks.[28,41,48,49] During MeOH dehydration, protonated clusters of methanol form around AlO$_4^-$ at high pressures, which inhibit MeOH dehydration at high pressures because some methanol must desorb prior to reactions occurring;[18] the same inhibitory regime occurs when the proximity of Al in the framework is

systematically altered.[9] Samples with higher fractions of paired Al also have higher rate constants for MeOH dehydration to DME (first-order, zero-order, and inhibitory) at 415 K from 0.5 to 60 kPa. The presence of inhibition and the higher rate constants on paired sites at all evaluated pressures indicate that clusters still form on paired sites, and the benefit conferred by pairing persists in the presence of these clusters; however, the structure of larger clusters (>2 ML, defined as MeOH per H$^+$) remains unexplored. We begin by studying the clustering of methanol molecules on NNN and NNNN Al pairs in the 6-MR of CHA.

In our prior study of methanol clustering at isolated BA sites in CHA,[18] we found that methanol clusters preferred to form protonated chains which interacted with the conjugate base of the deprotonated BA sites at both the ends of the chain. Based on our results on isolated BA sites, we focus here on methanol coverages of ≤6 ML. Because two sites are now present within the 6-MR, more complex structures can be formed and were examined in this work. For example, clusters can be present as a single branched chain (with a +2 charge) or can form two cationic chains that potentially have different lengths. These branched or independent chains can also interact with one or both conjugate bases of the BA sites simultaneously. These structural motifs were captured in this work, leading to structural optimizations of 145−1315 methanol chain arrangements for each coverage and Al arrangement (Table S8, Supporting Information). While AIMD simulations may permit for a large sampling of the potential energy surface and shed light on the dynamics of these clusters, such a large number of configurational tests should identify preferred configurations at a lower computational cost. Our focus will be on the most stable identified structures as these are expected to be dominant at the low temperatures relevant to methanol dehydration.

Our prior work[20] studying methanol dehydration on site pairs in CHA examined methanol coverages ≤2 MeOH/H$^+$; thus, we focus our discussion on larger clusters in this work. Generally, calculated energies indicate that two separate protonated clusters are preferred on NNN and NNNN pairs rather than one large cluster solvating the protons from both sites (Section S.4, Supporting Information). One methanol chain sits above the shared 6-MR and forms H-bonds to the conjugate bases of both BA sites in the most stable configuration at most coverages ≥1 ML and in all coverages from 1−4.5 ML. The ability for cations to interact simultaneously with two anionic conjugate base structures was also observed for transition-state structures and causes
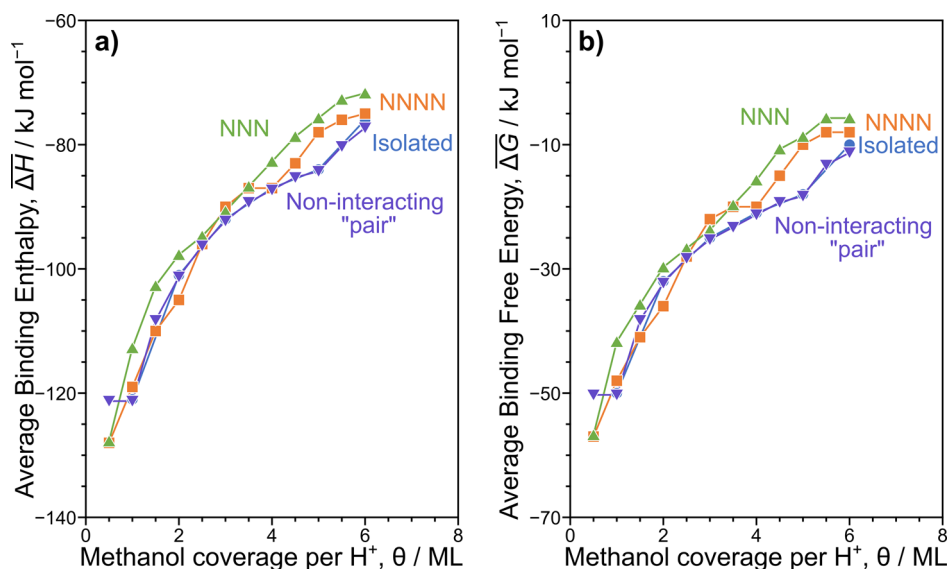
Figure 3. Average (a) binding enthalpies and (b) binding free energies for methanol coverages (θ) of 0.5−6 per H⁺ on isolated sites (blue, ●), NNN site-pairs (green, ▲), NNNN site-pairs (orange, ■), and a noninteracting "pair" of isolated sites (purple, ▼).

higher MeOH dehydration rate constants for paired Al in CHA.[9,20] The continued preference for these similar interactions between sites above the 6-MR suggests that they are also the source of higher rate constants in the inhibitory regime of MeOH dehydration on CHA. The chain above the shared 6-MR is comprised of two MeOH molecules for most structures at coverages from 2−4 ML on both NNN and NNNN site-pairs, while the remaining 2−6 MeOH form a second chain. This indicates that the two cationic chains interacting with the BA site pair are likely to be different sizes. For larger MeOH coverages, more than two chains can form. For example, the most stable configuration on the NNNN pair at 4 ML forms two distinct MeOH dimers above the 6-MR and a 6-MeOH chain in a nearby cage, the latter of which contains a cyclic network of H-bonded MeOH molecules similar to those observed in our studies of isolated BA sites (Figure 2b). Similar rings of methanol molecules within clusters form favorably at higher coverages on the NNNN site (Figure 2c−f), indicating that internal H-bonded rings are likely forming in the inhibitory regime of MeOH dehydration. These independent chains may alter the dynamics of MeOH desorption from chains to form transition states with the preferred molecularity; these desorption events cause inhibition in the kinetic data which persist on paired sites.

Average methanol binding energies remain similar between isolated and paired sites for coverages up to 6 ML (Figure 3). Here, we approximate the behavior of a "noninteracting pair", which is intended to simulate the behavior of two isolated sites to compare to paired sites more directly. The energy of the noninteracting pair is calculated from the sum of energies from a pair of isolated sites at given MeOH coverages ($E_{\text{iso},i}$) with the energy of a Si-form (E_{Si}) subtracted from that total to yield comparable energies to the single unit cell calculations with paired site configurations

$$E_{\text{nonint},i+j} = E_{\text{iso},i} + E_{\text{iso},j} - E_{\text{Si}} \qquad (7)$$

where i and j are the number of methanol molecules around the two sites, with a corresponding total coverage of $\frac{i+j}{2}$. E_{nonint} values for a given coverage were calculated with all possible

combinations of i and j, and binding energies are calculated from the lowest energy at a given coverage. Notably, the number of Si, Al, and O atoms accounted for in E_{nonint} are equivalent to those calculated directly on paired site models (i.e., the energies can be directly compared), with 34 framework Si, 2 Al, and 72 O atoms. The preferred combinations at a given coverage almost always were comprised of two isolated sites with the same number of MeOH (e.g., for θ = 3 MeOH per H⁺, $i = j = 3$). The only exception to this trend was when θ = 6, where the lowest noninteracting energy occurred when one site had 5 MeOH and the other had 7 MeOH. Because these energies are typically derived from two isolated sites with identical MeOH coverages, the average noninteracting binding energies overlap perfectly with binding energies at isolated sites (Figure 3). Binding energies on paired sites are stronger (more negative) at 0.5 ML, indicating that a methanol monomer binds more strongly to a BA site when a second BA site with a bare proton is nearby. This occurs because a H-bond forms between the two BA sites upon adsorption of MeOH (a weak base), as previously discussed.[20] Binding 1 MeOH per H⁺ (at 1 ML) results in a weaker average binding free energy for both NNN and NNNN pairs compared to the noninteracting pair because that H-bond between the two BA sites is broken. As dimers and larger chains form, the average binding free energies of the MeOH interacting with NNN and NNNN pairs are similar to those for isolated sites up to 4 ML, above which they are significantly weaker (less negative), indicating that there are steric limits that impact the formation of larger clusters for Al pairs.

3.3. Microkinetic Modeling

The continued presence of H-bonding interactions between paired sites with larger clusters present and the larger rate constants on paired sites compared to those on isolated sites in the inhibitory regime of MeOH dehydration above 20 kPa indicate that reductions in barriers from isolated to paired sites should be similar regardless of MeOH coverage, including with larger clusters present. As such, the microkinetic model in this work was parameterized by using as input the potential energy landscapes of the sequential and concerted pathways over the

Table 1. List of DFT-Calculated Parameters That Were Tuned During Parameter Optimization[a,b]

Parameter	A (s^{-1} or $(Pa\ s)^{-1}$)	E_a (kJ/mol)	original $k(T)$	tuned parameter	tuned $k(T)$
$k_{iso,elim}$	$8.64 \times 10^{12}\ s^{-1}$	129.5	$4.33 \times 10^{-4}\ s^{-1}$	E_a, 123.5 kJ/mol	$2.46 \times 10^{-3}\ s^{-1}$
$k_{pair,elim}$	$8.64 \times 10^{12}\ s^{-1}$	128.8	$5.30 \times 10^{-4}\ s^{-1}$	E_a, 122.8 kJ/mol	$3.02 \times 10^{-3}\ s^{-1}$
$k_{pair,conc,dim}$	$8.64 \times 10^{12}\ s^{-1}$	127.0	$8.93 \times 10^{-4}\ s^{-1}$	E_a, 121.0 kJ/mol	$5.08 \times 10^{-3}\ s^{-1}$
$k_{iso,trim}$	$1.37 \times 10^{3}\ (Pa\ s)^{-1}$	0	$1.37 \times 10^{3}\ (Pa\ s)^{-1}$	A, $1.37 \times 10^{4}\ (Pa\ s)^{-1}$	$1.37 \times 10^{4}\ (Pa\ s)^{-1}$
$k_{pair,trim}$	$1.66 \times 10^{3}\ (Pa\ s)^{-1}$	0	$1.66 \times 10^{3}\ (Pa\ s)^{-1}$	A, $1.66 \times 10^{4}\ (Pa\ s)^{-1}$	$1.66 \times 10^{4}\ (Pa\ s)^{-1}$
$k_{iso,conc,trim}$	$8.64 \times 10^{12}\ s^{-1}$	120.5	$5.88 \times 10^{-3}\ s^{-1}$	E_a, 121.8 kJ/mol	$4.03 \times 10^{-3}\ s^{-1}$
$k_{pair,conc,trim}$	$8.64 \times 10^{12}\ s^{-1}$	111.0	$9.22 \times 10^{-2}\ s^{-1}$	E_a, 107.0 kJ/mol	$2.94 \times 10^{-1}\ s^{-1}$
$k_{iso,tet}$	$1.22 \times 10^{3}\ (Pa\ s)^{-1}$	0	$1.22 \times 10^{3}\ (Pa\ s)^{-1}$	A, $3.51 \times 10^{2}\ (Pa\ s)^{-1}$	$3.51 \times 10^{2}\ (Pa\ s)^{-1}$
$k_{pair,tet}$	$5.72 \times 10^{2}\ (Pa\ s)^{-1}$	0	$5.72 \times 10^{2}\ (Pa\ s)^{-1}$	A, $5.72 \times 10^{3}\ (Pa\ s)^{-1}$	$5.72 \times 10^{3}\ (Pa\ s)^{-1}$
$k_{iso,pent}$	$1.05 \times 10^{3}\ (Pa\ s)^{-1}$	0	$1.05 \times 10^{3}\ (Pa\ s)^{-1}$	A, $1.05 \times 10^{2}\ (Pa\ s)^{-1}$	$1.05 \times 10^{2}\ (Pa\ s)^{-1}$
$k_{pair,pent}$	$5.72 \times 10^{2}\ (Pa\ s)^{-1}$	0	$5.72 \times 10^{2}\ (Pa\ s)^{-1}$	A, $5.53 \times 10^{3}\ (Pa\ s)^{-1}$	$5.53 \times 10^{3}\ (Pa\ s)^{-1}$

[a]E_a values were tuned for relevant elementary steps where possible and A values for adsorption events that are unactivated in our model framework. Values are reported at 415 K. [b]Note that the experimental data used was at a fixed temperature (415 K), and thus, adjustments to k values through A or E_a are indistinguishable. Data at multiple temperatures would be required to explore these individual changes further, allowing the impact of varying an activation energy versus a pre-exponential factor to be distinguished. Nevertheless, all changes to the parameters were well within the bounds set by adjustments permitted to theoretical values based on inherent DFT errors.
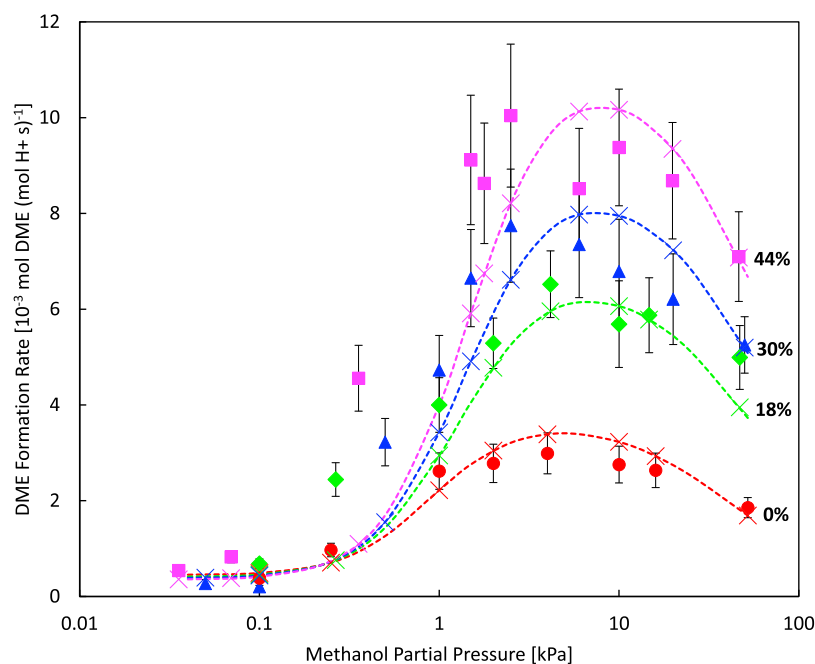

Figure 4. Comparison of model output and experimental values for the full range of MeOH partial pressures and paired acid site fractions for 0% paired acid sites (red, ●), 18% paired acid sites (green, ♦), 30% paired acid sites (blue, ▲), and 44% paired acid sites (pink, ■). Markers with error bars are the experimental data from Di Iorio et al.[8] adjusted as described in Section S.2, Supporting Information. The crosses identify the output of individual microkinetic model runs at the given paired acid site percentages at methanol partial pressures matching each experimental data point. The dashed lines connecting microkinetic model outputs are presented to guide the eye.

isolated and paired acid sites. Reaction rate coefficients were formulated in the Arrhenius form (Equation 8), with a pre-exponential factor (A) and activation energy (E_a) specified for each reaction. The calculated enthalpies and free energies (and corresponding entropies) of reactant, intermediate, and product states along the reaction coordinate of concerted and sequential pathways were used to estimate the kinetic parameters and pre-exponential factors for each elementary step, ensuring thermodynamic consistency. The effect of methanol clustering over both paired and isolated active sites was accounted for explicitly, up to 5 methanol molecules per active site. Di Iorio et al.[18] have examined the two competing pathways through a combination of experiments and electronic structure calculations, with a focus on the presence of spectator

species, expected to be a part of higher-order clusters around acid sites at larger partial pressures of methanol.

$$k(T) = A \times e^{(-E_a/RT)} \tag{8}$$

In this work, we extend the analysis of DME formation in the presence of spectator species to involve the paired acid site configurations as distinct active sites. Generally, the ground states of reactants were found to be less stable on paired sites when compared to analogous structures over isolated active sites, especially with the increase in methanol cluster size. The values of these differences in ground state stabilities were on the order of 5−15 kJ/mol. In addition, the relative energies of the product states were found to be more stable relative to their analogues over isolated sites (22−28 kJ/mol). This could
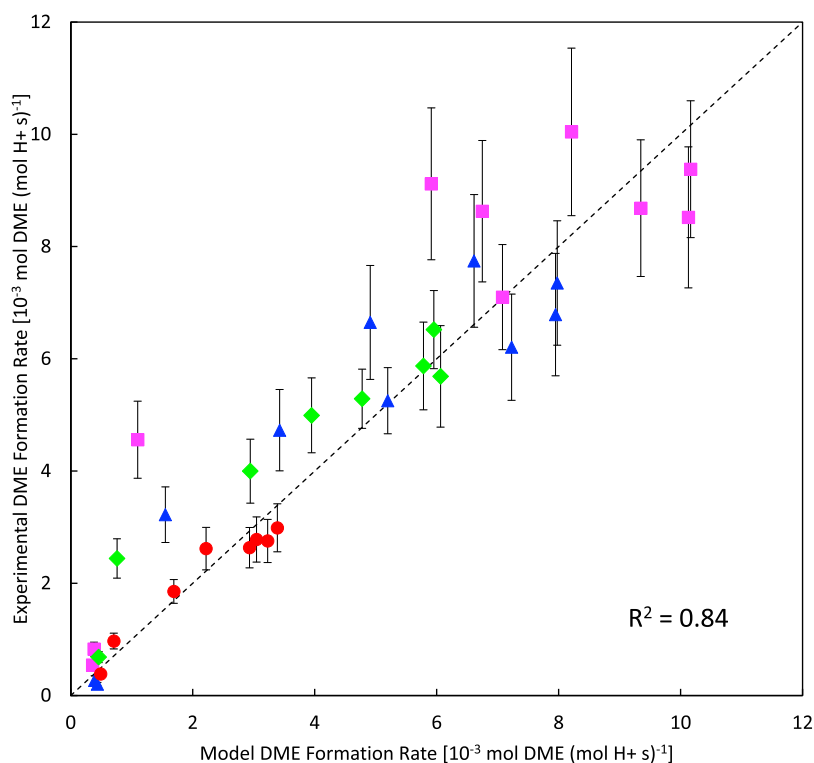
Figure 5. Parity plot comparing the model output and value for experimental rate law from the data of Di Iorio et al.[8] at all considered methanol partial pressure conditions for 0% paired acid sites (red, ●), 18% paired acid sites (green, ♦), 30% paired acid sites (blue, ▲), and 44% paired acid sites (pink, ■).

be rationalized by favorable hydrogen bond networks formed in the presence of paired acid sites, relative to the case of isolated-only sites. The effect of methanol clustering on paired acid site configurations can be exemplified in terms of activation free energies of the concerted pathway, with the values of 127.0, 110.0, and 131.5 kJ/mol corresponding to transition states with zero, one, and two spectator methanol molecules, respectively. For comparison, when examining the most stable isolated active site structure from conformational analysis, the activation free energies with zero, one, and two spectator species were calculated to be 137.0, 120.5, and 146.0 kJ/mol, respectively. Desorption events were assumed to be activated, with the enthalpy of adsorption used as the activation energy. The complete set of adsorption enthalpies, activation free energies, and associated first-order rate constants for the concerted and sequential pathways, as summarized in Scheme 1, is reported in Table S1 of the Supporting Information.

The experimental methanol dehydration rate values reported previously by Di Iorio et al.[9] on H-CHA zeolites were scaled down by a factor of 3.6 times to account for updated product response factors in the gas chromatograph flame ionization detector in the experimental setup used (additional details in Section S.2, Supporting Information). The parameters derived from DFT (reported in Table S1 of the Supporting Information) were used to simulate initial DME formation rate as a function of pressure (0.04−52.09 kPa CH$_3$OH) for CHA samples ranging from entirely isolated sites to 44% paired acid sites. The experimental Co^{2+} titration method is unable to distinguish between NNN and NNNN sites in the 6-MR of CHA, so two initial simulations were run assuming either all NNN or all NNNN sites (Figures S2 and S3 in the Supporting Information). With the parameterization of the

DFT data, NNNN sites were shown to have negligible impact on DME formation, even when tuning parameters within typical DFT uncertainty (Figure S4 in the Supporting Information). A mixture of 7.4% NNN to 92.6% NNNN sites was then assumed to match the results for relative Al−Al site probabilities for the 6-MR in CHA from simulations performed by Di Iorio et al.,[13] and NNNN sites were assumed to have negligible flux with respect to DME formation. As described in Section 2.2, parameters to which the model was most sensitive were adjusted, and the final set of those parameters that were varied is shown in Table 1.

The microkinetic modeling results obtained using the tuned reaction parameters are shown in Figure 4, displaying good agreement with the experimental data at pressures below 0.1 kPa and above 1 kPa. A parity plot is shown in Figure 5 with an R^2 value of 0.84. The model nicely captures the peak in the rate as a function of pressure due to large methanol cluster inhibition at all fractions of paired sites, and the separation between the curves, with the total rate increasing with the increase in the fraction of paired sites, is recapitulated well.

3.4. Degree of Rate Control Analysis

A quantitative analysis was performed of the DME formation rates obtained as output from the microkinetic model to understand how the changes in activation free energies of elementary steps along the potential energy surface affect the overall reaction rate. Application of this type of sensitivity analysis allows for the identification of the elementary step(s) that control overall reaction rates.[50−53] The metric used in the analysis of the degree of rate control for an elementary step i is the sensitivity coefficient (X_i), which is defined by Campbell[54] as eq 9
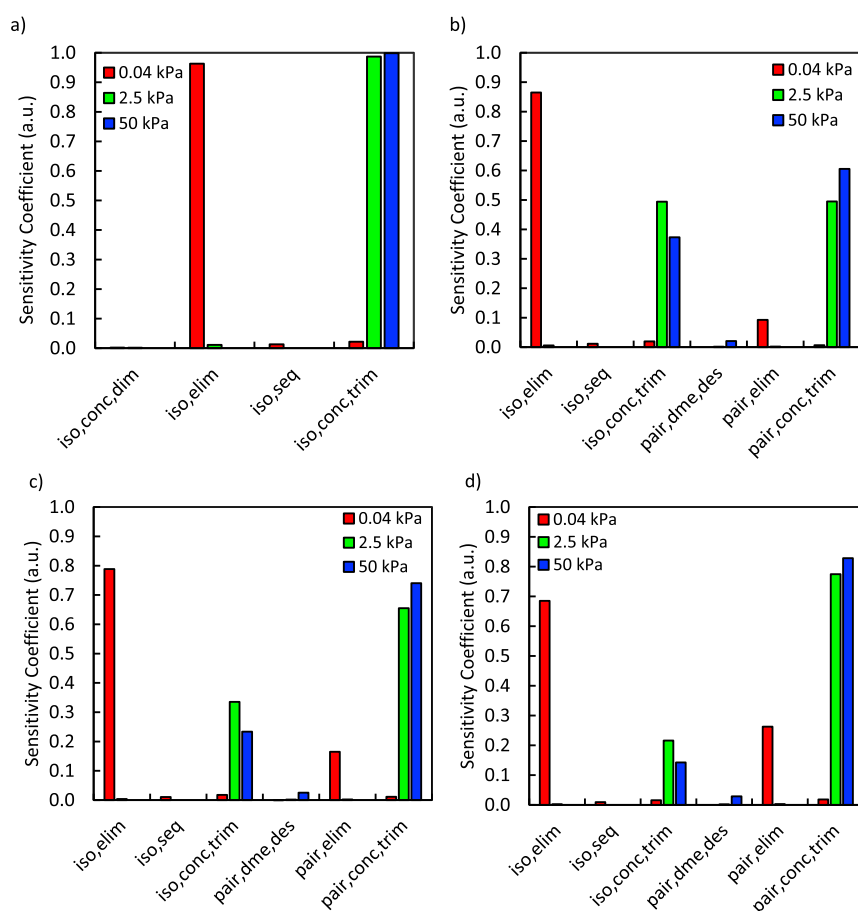
Figure 6. Calculated DRC sensitivity coefficients for (a) 0% paired acid sites, (b) 18% paired acid sites, (c) 30% paired acid sites, and (d) 44% paired acid sites at MeOH partial pressures of 0.04, 2.5, and 50 kPa. All relevant elementary steps are reported using the same notation as in Scheme 1.

$$X_i = \frac{k_i}{r}\left(\frac{\partial r}{\partial k_i}\right)_{k_{j\neq i}, K_i} = \left(\frac{\partial \ln(r)}{\partial \ln(k_i)}\right)_{k_{j\neq i}, K_i} = \left(\frac{\partial \ln(r)}{\partial\left(\frac{-\Delta G_i^{TS}}{RT}\right)}\right)_{k_{j\neq i}, K_i} \quad (9)$$

where r is the net rate of formation of the product of interest, which in this case is taken to be DME. Equation 9 was applied to the full set of rate constants in the case of isolated-only and mixed isolated-paired site configurations for a range of reactant feed partial pressures. Figure 6 reports the calculated sensitivity coefficients for the cases of isolated-only and binary mixtures containing 18−44% paired acid sites at a temperature of 415 K. Three representative feed partial pressures of MeOH were chosen—namely, 0.04, 2.5, and 50 kPa. Different elementary steps (and corresponding mechanisms) are rate-controlling in different MeOH partial pressure regimes. For example, the water elimination/alkoxide formation ($k_{\text{iso,elim}}$ and $k_{\text{pair,elim}}$) step of the dissociative pathway is rate-controlling at low MeOH partial pressures (0.04 kPa—red), while direct DME formation from the methanol trimer state ($k_{\text{iso,conc,trim}}$ and $k_{\text{pair,conc,trim}}$), via the associative mechanism, became rate-controlling at greater pressures (2.5−50 kPa—green, blue). This is mostly consistent with prior rate estimations on isolated sites in CHA using maximum rate analysis—which assumes only one prevailing rate-determining step as a heuristic for determining a mechanism rather than determining degrees of rate con-

trol—based on DFT-calculated barriers. This analysis showed that methanol dehydration proceeds primarily via the dissociative mechanism below 0.3 kPa MeOH at 415 K and via the associative mechanism with one spectating methanol above 0.3 kPa.[18] The calculated X_i values indicate that the extent of degree of rate control for the elementary steps considered is a function of the paired site concentration. As the total fraction of paired active sites increased, the calculated X_i values increased proportionately for all elementary steps occurring over paired sites (Figure 6b−d).

In summary, DME formation from the trimer state appears to be rate-controlling for most reactant feed partial pressures and active site configurations (Figure 6). This can be attributed to the unique case of trimer states along the potential energy surface of the associative pathway, in which the favorable molecular arrangement results in low reaction barriers and contributes the majority of DME flux at steady state. These trimeric transition states appear to optimize H-bonding between the species in the transition state and the conjugate base, as illustrated by transition states found in previous work[18] on isolated sites in CHA (Figure 7). Only at very low reactant partial pressures does the dissociative mechanism participate in DME formation chemistry, as demonstrated by the calculated X_i values. Conversely, at high reactant partial pressures, the calculated X_i values indicate the trimer state as rate-controlling with calculated values of 0.61−0.83 for paired site fractions of 18−44%. Negligible rates and corresponding X_i values were observed for reactions preceded
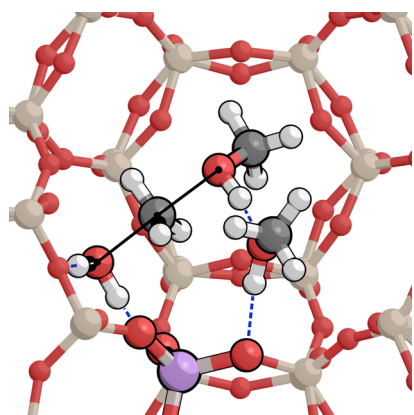
Figure 7. Structure of the trimeric concerted methanol dehydration transition state that likely prevails at most conditions, shown here on an isolated site (first described in our previous work).[18] Incipient and breaking bonds are shown with solid black lines, and H-bonds are shown with dashed blue lines.

by tetramer formation, further highlighting the importance of the favorable molecular conformation in the dimer and trimer states. The full set of X_i values calculated for the full range of MeOH partial pressures and paired site fractions is reported in the Supporting Information.

3.5. Reaction Flux and Surface Speciation Analysis

Snapshots of the reactor design equation solutions at the correct isolated site basis along the PFR integration were taken to identify flux through reaction pathways. Flux partitions itself to the two sides (namely, the concerted and sequential pathways) of the mechanism shown in Scheme 1. As shown in Figure 8a, looking first solely at isolated sites, the sequential pathway dominates at very low methanol partial pressures. As methanol pressure increases, the concerted pathway begins to express with flux through the trimer pathway. As initial methanol pressure continues to increase, the trimer pathway dominates strongly, and the tetramer pathway is never noticeably expressed at any pressure condition. In examining the speciation on the isolated sites under the same conditions as the flux mapped in Figure 8a, an interesting result is seen in Figure 9. At a methanol pressure of 1000 Pa, bound methanol trimers have nearly equal speciation with the combination of methanol monomers and dimers. However, the trimer pathway completely dominates the mechanism at this pressure due in part to the much lower activation energy for the concerted trimer ($k_{conc,trim}$) steps compared to the concerted tetramer ($k_{conc,tet}$) and concerted dimer ($k_{conc,dim}$) steps, even prior to any tuning of the DFT values. The tetramer pathway shows no significant contribution to the overall DME flux, even at conditions where tetramers make up a significant portion of the speciation, such as 50 kPa methanol. Notably, the primary bound species present are the bound methanol monomers,
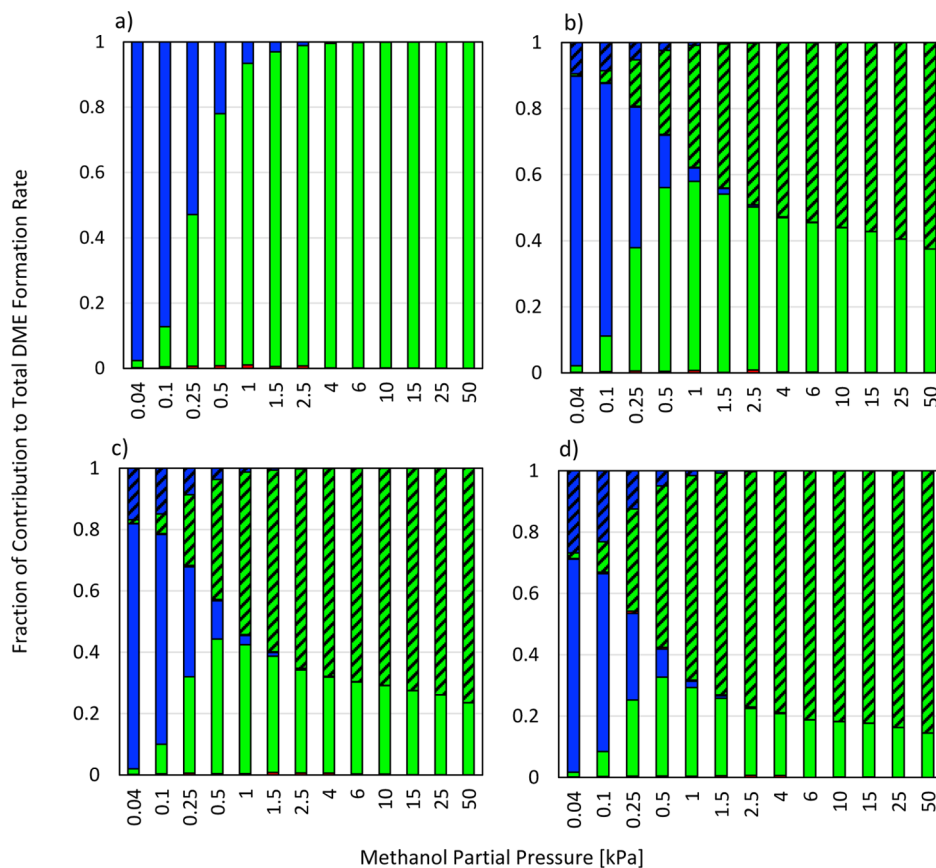
Figure 8. Fraction of each primary branch of the mechanism's contribution to the overall DME production for (a) 0% paired acid sites, (b) 18% paired acid sites, (c) 30% paired acid sites, and (d) 44% paired acid sites. Red: contribution from MeOH dimer pathway. Green: contribution from MeOH trimer pathway. Blue: contribution from sequential pathway. Unshaded bars correspond to contributions from isolated acid sites, whereas shaded bars correspond to contributions coming from paired acid sites.
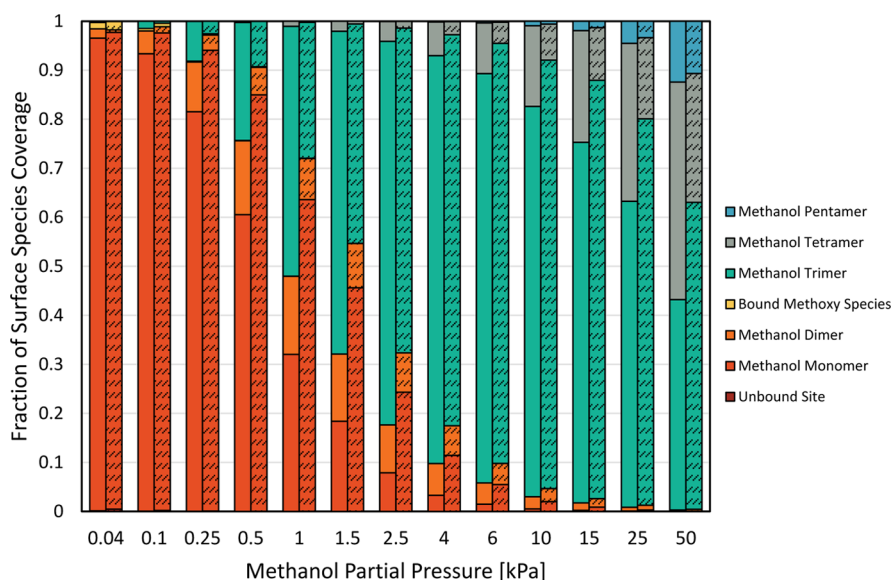
Figure 9. Surface species coverage at various MeOH partial pressures at the outlet of the simulated PFR. Methanol monomers dominate the speciation at lower pressures, with trimers and tetramers becoming most prevalent as methanol partial pressure rises to 50 kPa. Left: isolated acid sites. Right (shaded): paired acid sites.

dimers, trimers, tetramers, and pentamers as well as the methoxy species indicative of the sequential pathways. All other surface species are only present in negligible amounts.

Figure 8b–d shows the partitioning of the flux as a function of methanol partial pressure as the number of paired sites increases. Paired sites display similar flux behavior to isolated sites, though their rates are higher and thus their contribution to the total is significant. Note that four major categories of fluxes can be gleaned from these figures: sequential on isolated sites, sequential on paired sites, concerted on isolated sites (primarily through MeOH trimers), and concerted on paired sites. It is clear from the variety of contributions in Figure 8b–d that the total rate of DME production captured in Figure 4 is a complex amalgam of these routes, the contributions of which change as the reaction conditions change. At low methanol pressure, the sequential pathway dominates despite the low absolute coverage of methoxy species shown in Figure 9 due to the even lower coverage of the trimer species that promote the rapid concerted pathway. As methanol partial pressure increases, the dimer and trimer pathways become expressed, ultimately resulting in the paired trimer pathway dominating the overall DME flux for the system at high pressure conditions.

The speciation as a function of MeOH partial pressure and fraction of paired sites is shown in Figure 9. In the presence of paired sites, isolated sites show no significant differences in speciation or numerical contribution to flux. Paired sites also show consistent speciation at different ratios of isolated sites to paired sites. At the pressure conditions investigated, monomers dominate at a low pressure but are replaced by trimers as pressure increases. Bound dimer species are generally less prominent on paired sites compared to isolated sites. Tetramer and pentamer species also express lower percentages at high methanol partial pressure conditions on paired sites, with methanol trimers dominating the surface at methanol partial pressures ranging from 1.5 to 50 kPa. Given that the trimer pathway is identified to be responsible for the majority of flux in the isolated case and that the tetramer pathway shows little to no flux contribution despite high surface concentration, this

higher trimer surface concentration partly accounts for the overall higher DME flux of paired sites in comparison to isolated sites along with the more beneficial activation energies along the trimer pathway for paired active sites.

In summary, the speciation and flux analyses identify the MeOH trimer pathway to be the dominant pathway for DME production. Trimers form more readily on paired acid sites at high MeOH partial pressures in comparison to inactive tetramers and pentamers while dominating the surface coverage, which when paired with the lower energy barriers along the trimer pathway for paired active sites rationalizes the higher DME formation turnover rates (per H^+) identified on paired acid sites.

4. CONCLUSIONS

In this work, we present a DFT-parameterized microkinetic model that captures and identifies the effects of acid site proximity in CHA on methanol dehydration rates. Through flux analysis and surface species identification, we identify two primary drivers of methanol dehydration chemistry. At methanol pressures below 250 Pa, a sequential pathway through a bound methoxy intermediate dominates. Above 250 Pa of methanol pressure, the rapid formation of methanol trimer clusters causes a shift in the flux through the concerted trimer pathway. NNN paired acid sites promote the formation of trimer species over inhibiting tetramer or pentamer clusters and have lower energy barriers presented in the concerted trimer pathway, resulting in the large increase in the rate of DME production for this class of sites. This modeling methodology and framework can be extended to capture the effects of paired active site chemistry on additional zeolite frameworks beyond CHA and on chemistries beyond methanol dehydration, aiding in the development of next-generation catalysts.

ASSOCIATED CONTENT

Supporting Information

The Supporting Information is available free of charge at https://pubs.acs.org/doi/10.1021/acsmaterialsau.1c00057.

All DFT-evaluated parameters for isolated, NNN, and NNNN sites within the 6-member ring of chabazite zeolite; microkinetic modeling results for untuned DFT parameters in comparison to experimental data on fully NNN paired sites, fully NNNN paired sites, and a ratio of 7.4% NNN sites to 92.6% NNNN sites, as well as maximally tuned DFT parameters for fully NNNN paired sites; DRC sensitivity coefficients for paired acid site percentages ranging from 0 to 44%; benchmarking of methanol dehydration turnover rates and kinetic parameters with commercial MFI samples; calculation of H, G, and S through statistical mechanics; configurational analysis of cluster methanol cluster sizes; and DFT calculations of methanol cluster structures (PDF)

AUTHOR INFORMATION

Corresponding Author

Linda J. Broadbelt — *Department of Chemical and Biological Engineering, Northwestern University, Evanston, Illinois 60208, United States;* orcid.org/0000-0003-4253-592X; Email: broadbelt@northwestern.edu

Authors

Grant Marsden — *Department of Chemical and Biological Engineering, Northwestern University, Evanston, Illinois 60208, United States*

Pavlo Kostetskyy — *Department of Chemical and Biological Engineering, Northwestern University, Evanston, Illinois 60208, United States;* orcid.org/0000-0003-2796-0362

Ryoh-Suke Sekiya — *Department of Chemical Engineering, University of Florida, Gainesville, Florida 32611, United States*

Alexander Hoffman — *Department of Chemical Engineering, University of Florida, Gainesville, Florida 32611, United States;* orcid.org/0000-0002-1337-9297

Songhyun Lee — *Charles D. Davidson School of Chemical Engineering, Purdue University, West Lafayette, Indiana 47907, United States*

Rajamani Gounder — *Charles D. Davidson School of Chemical Engineering, Purdue University, West Lafayette, Indiana 47907, United States;* orcid.org/0000-0003-1347-534X

David Hibbitts — *Department of Chemical Engineering, University of Florida, Gainesville, Florida 32611, United States;* orcid.org/0000-0001-8606-7000

Complete contact information is available at:
https://pubs.acs.org/10.1021/acsmaterialsau.1c00057

Notes

The authors declare no competing financial interest.

ACKNOWLEDGMENTS

REFERENCES

(1) Haag, W. O.; Lago, R. M.; Weisz, P. B. The active site of acidic aluminosilicate catalysts. *Nature* **1984**, *309*, 589−591.

(2) Dusselier, M.; Davis, M. E. Small-Pore Zeolites: Synthesis and Catalysis. *Chem. Rev.* **2018**, *118*, 5265−5329.

(3) Shamzhy, M.; Opanasenko, M.; Concepción, P.; Martínez, A. New trends in tailoring active sites in zeolite-based catalysts. *Chem. Soc. Rev.* **2019**, *48*, 1095−1149.

(4) Corma, A. Inorganic Solid Acids and Their Use in Acid-Catalyzed Hydrocarbon Reactions. *Chem. Rev.* **1995**, *95*, 559−614.

(5) Berkson, Z. J.; Hsieh, M. F.; Smeets, S.; Gajan, D.; Lund, A.; Lesage, A.; Xie, D.; Zones, S. I; McCusker, L. B.; Baerlocher, C.; Chmelka, B. F. Preferential Siting of Aluminum Heteroatoms in the Zeolite Catalyst Al-SSZ-70. *Angew. Chem., Int. Ed.* **2019**, *58*, 6255−6259.

(6) Dedecek, J.; Balgová, V.; Pashkova, V.; Klein, P.; Wichterlová, B. Synthesis of ZSM-5 Zeolites with Defined Distribution of Al Atoms in the Framework and Multinuclear MAS NMR Analysis of the Control of Al Distribution. *Chem. Mater.* **2012**, *24*, 3231−3239.

(7) Dedecek, J.; Sobalik, Z.; Wichterlova, B. Siting and Distribution of Framework Aluminium Atoms in Silicon-Rich Zeolites and Impact on Catalysis. *Catal. Rev.: Sci. Eng.* **2012**, *54*, 135−223.

(8) Di Iorio, J. R.; Gounder, R. Controlling the Isolation and Pairing of Aluminum in Chabazite Zeolites Using Mixtures of Organic and Inorganic Structure-Directing Agents. *Chem. Mater.* **2016**, *28*, 2236−2247.

(9) Di Iorio, J. R.; Nimlos, C. T.; Gounder, R. Introducing Catalytic Diversity into Single-Site Chabazite Zeolites of Fixed Composition via Synthetic Control of Active Site Proximity. *ACS Catal.* **2017**, *7*, 6663−6674.

(10) Li, C.; Vidal-Moya, A.; Miguel, P. J.; Dedecek, J.; Boronat, M.; Corma, A. Selective Introduction of Acid Sites in Different Confined Positions in ZSM-5 and Its Catalytic Implications. *ACS Catal.* **2018**, *8*, 7688−7697.

(11) Mlekodaj, K.; Dedecek, J.; Pashkova, V.; Tabor, E.; Klein, P.; Urbanova, M.; Karcz, R.; Sazama, P.; Whittleton, S. R.; Thomas, H. M.; Fishchuk, A. V.; Sklenak, S. Al Organization in the SSZ-13 Zeolite. Al Distribution and Extraframework Sites of Divalent Cations. *J. Phys. Chem. C* **2019**, *123*, 7968−7987.

(12) Wang, S.; He, Y.; Jiao, W.; Wang, J.; Fan, W. Recent experimental and theoretical studies on Al siting/acid site distribution in zeolite framework. *Curr. Opin. Chem. Eng.* **2019**, *23*, 146−154.

(13) Di Iorio, J. R.; Li, S.; Jones, C. B.; Nimlos, C. T.; Wang, Y.; Kunkes, E.; Vattipalli, V.; Prasad, S.; Moini, A.; Schneider, W. F.; Gounder, R. Cooperative and Competitive Occlusion of Organic and Inorganic Structure-Directing Agents within Chabazite Zeolites Influences Their Aluminum Arrangement. *J. Am. Chem. Soc.* **2020**, *142*, 4807−4819.

(14) Devos, J.; Bols, M. L.; Plessers, D.; Goethem, C. V.; Seo, J. W.; Hwang, S.-J.; Sels, B. F.; Dusselier, M. Synthesis−Structure−Activity Relations in Fe-CHA for C−H Activation: Control of Al Distribution by Interzeolite Conversion. *Chem. Mater.* **2020**, *32*, 273−285.

(15) Liang, Y.; Jacobson, A. J.; Rimer, J. D. Strontium Ions Function as Both an Accelerant and Structure-Directing Agent of Chabazite Crystallization. *ACS Mater. Lett.* **2021**, *3*, 187−192.

(16) Loewenstein, W. The distribution of aluminum in the tetrahedra of silicates and aluminates. *Am. Mineral.* **1954**, *39*, 92−96.

(17) Gounder, R.; Jones, A. J.; Carr, R. T.; Iglesia, E. Solvation and acid strength effects on catalysis by faujasite zeolites. *J. Catal.* **2012**, *286*, 214−223.

(18) Di Iorio, J. R.; Hoffman, A. J.; Nimlos, C. T.; Nystrom, S.; Hibbitts, D.; Gounder, R. Mechanistic origins of the high-pressure inhibition of methanol dehydration rates in small-pore acidic zeolites. *J. Catal.* **2019**, *380*, 161−177.

(19) Vernuccio, S.; Bickel, E. E.; Gounder, R.; Broadbelt, L. J. Microkinetic Model of Propylene Oligomerization on Bronsted Acidic Zeolites at Low Conversion. *ACS Catal.* **2019**, *9*, 8996−9008.

(20) Hoffman, A. J.; Bates, J. S.; Di Iorio, J. R.; Nystrom, S. V.; Nimlos, C. T.; Gounder, R.; Hibbitts, D. Rigid Arrangements of Ionic Charge in Zeolite Frameworks Conferred by Specific Aluminum Distributions Preferentially Stabilize Alkanol Dehydration Transition States. *Angew. Chem., Int. Ed.* **2020**, *59*, 18686−18694.

(21) Smith, A. T.; Plessow, P. N.; Studt, F. Trends in the Reactivity of Proximate Aluminum Sites in H-SSZ-13. *J. Phys. Chem. C* **2021**, *125*, 16508−16515.

(22) Nastase, S. A. F.; Cnudde, P.; Vanduyfhuys, L.; De Wispelaere, K.; Van Speybroeck, V.; Catlow, C. R. A.; Logsdail, A. J. Mechanistic Insight into the Framework Methylation of H-ZSM-5 for Varying Methanol Loadings and Si/Al Ratios Using First-Principles Molecular Dynamics Simulations. *ACS Catal.* **2020**, *10*, 8904−8915.

(23) Baerlocher, C.; McCusker, L. B. Database of Zeolite Structures (accessed Aug 2020) http://www.iza-structure.org/databases/.

(24) Bräuer, P.; Ng, P. L.; Situmorang, O.; Hitchcock, I.; D'Agostino, C. Effect of Al content on number and location of hydroxyl acid species in zeolites: a DRIFTS quantitative protocol without the need for molar extinction coefficients. *RSC Adv.* **2017**, *7*, 52604−52613.

(25) Nystrom, S.; Hoffman, A.; Hibbitts, D. Tuning Bronsted Acid Strength by Altering Site Proximity in CHA Framework Zeolites. *ACS Catal.* **2018**, *8*, 7842−7860.

(26) Carr, R. T.; Neurock, M.; Iglesia, E. Catalytic consequences of acid strength in the conversion of methanol to dimethyl ether. *J. Catal.* **2011**, *278*, 78−93.

(27) Jones, A. J.; Zones, S. I.; Iglesia, E. Implications of Transition State Confinement within Small Voids for Acid Catalysis. *J. Phys. Chem. C* **2014**, *118*, 17787−17800.

(28) Bates, J. S.; Bukowski, B. C.; Greeley, J.; Gounder, R. Structure and solvation of confined water and water-ethanol clusters within microporous Bronsted acids and their effects on ethanol dehydration catalysis. *Chem. Sci.* **2020**, *11*, 7102−7122.

(29) Kresse, G.; Furthmüller, J. Efficiency of ab-initio total energy calculations for metals and semiconductors using a plane-wave basis set. *Comput. Mater. Sci.* **1996**, *6*, 15−50.

(30) Kresse, G.; Furthmüller, J. Efficient iterative schemes for ab initio total-energy calculations using a plane-wave basis set. *Phys. Rev. B: Condens. Matter Mater. Phys.* **1996**, *54*, 11169−11186.

(31) Kravchenko, P.; Plaisance, C.; Hibbitts, D. A New Computational Interface for Catalysis. ChemRxiv. [Preprint.] July 12, 2019 (accessed Nov 17, 2021) https://dx.doi.org/10.26434/chemrxiv.804073.v4.

(32) Kresse, G.; Joubert, D. From ultrasoft pseudopotentials to the projector augmented-wave method. *Phys. Rev. B: Condens. Matter Mater. Phys.* **1999**, *59*, 1758−1775.

(33) Blöchl, P. E. Projector augmented-wave method. *Phys. Rev. B: Condens. Matter Mater. Phys.* **1994**, *50*, 17953−17979.

(34) Grimme, S.; Ehrlich, S.; Goerigk, L. Effect of the Damping Function in Dispersion Corrected Density Functional Theory. *J. Comput. Chem.* **2011**, *32*, 1456−1465.

(35) Grimme, S.; Antony, J.; Ehrlich, S.; Krieg, H. A consistent and accurate ab initio parametrization of density functional dispersion correction (DFT-D) for the 94 elements H-Pu. *J. Chem. Phys.* **2010**, *132*, 154104.

(36) Hoffman, A.; Deluca, M.; Hibbitts, D. Restructuring of MFI Framework Zeolite Models and Their Associated Artifacts in Density Functional Theory Calculations. *J. Phys. Chem. C* **2019**, *123*, 6572−6585.

(37) Deluca, M.; Kravchenko, P.; Hoffman, A.; Hibbitts, D. Mechanism and Kinetics of Methylating C6−C12 Methylbenzenes with Methanol and Dimethyl Ether in H-MFI Zeolites. *ACS Catal.* **2019**, *9*, 6444−6460.

(38) Grifoni, E.; Piccini, G.; Lercher, J. A.; Glezakou, V.-A.; Rousseau, R.; Parrinello, M. Confinement effects and acid strength in zeolites. *Nat. Commun.* **2021**, *12*, 2630.

(39) Wang, M.; Jaegers, N. R.; Lee, M.-S.; Wan, C.; Hu, J. Z.; Shi, H.; Mei, D.; Burton, S. D.; Camaioni, D. M.; Gutiérrez, O. Y.; Glezakou, V.-A.; Rousseau, R.; Wang, Y.; Lercher, J. A. Genesis and Stability of Hydronium Ions in Zeolite Channels. *J. Am. Chem. Soc.* **2019**, *141*, 3444−3455.

(40) Alexopoulos, K.; Lee, M.-S.; Liu, Y.; Zhi, Y.; Liu, Y.; Reyniers, M.-F.; Marin, G. B.; Glezakou, V.-A.; Rousseau, R.; Lercher, J. A. Anharmonicity and Confinement in Zeolites: Structure, Spectroscopy, and Adsorption Free Energy of Ethanol in H-ZSM-5. *J. Phys. Chem. C* **2016**, *120*, 7172−7182.

(41) Bukowski, B. C.; Bates, J. S.; Gounder, R.; Greeley, J. Defect-Mediated Ordering of Condensed Water Structures in Microporous Zeolites. *Angew. Chem., Int. Ed.* **2019**, *58*, 16422−16426.

(42) Bukowski, B. C.; Bates, J. S.; Gounder, R.; Greeley, J. First principles, microkinetic, and experimental analysis of Lewis acid site speciation during ethanol dehydration on Sn-Beta zeolites. *J. Catal.* **2018**, *365*, 261−276.

(43) McQuarrie, D. A. *Statistical Mechanics*; University Science Books: Sausalito, California, 2000; pp 129−140.

(44) Ghorbanpour, A.; Rimer, J. D.; Grabow, L. C. Computational Assessment of the Dominant Factors Governing the Mechanism of Methanol Dehydration over H-ZSM-5 with Heterogeneous Aluminum Distribution. *ACS Catal.* **2016**, *6*, 2287−2298.

(45) Mei, D.; Lercher, J. A. Mechanistic insights into aqueous phase propanol dehydration in H-ZSM-5 zeolite. *AIChE J.* **2017**, *63*, 172−184.

(46) Jones, A. J.; Iglesia, E. Kinetic, Spectroscopic, and Theoretical Assessment of Associative and Dissociative Methanol Dehydration Routes in Zeolites. *Angew. Chem., Int. Ed.* **2014**, *53*, 12177−12181.

(47) Mirth, G.; Lercher, J. A.; Anderson, M. W.; Klinowski, J. Adsorption complexes of methanol on zeolite ZSM-5. *J. Chem. Soc., Faraday Trans.* **1990**, *86*, 3039−3044.

(48) Vjunov, A.; Wang, M.; Govind, N.; Huthwelker, T.; Shi, H.; Mei, D.; Fulton, J. L.; Lercher, J. A. Tracking the Chemical Transformations at the Brønsted Acid Site upon Water-Induced Deprotonation in a Zeolite Pore. *Chem. Mater.* **2017**, *29*, 9030−9042.

(49) Eckstein, S.; Hintermeier, P. H.; Zhao, R.; Baráth, E.; Shi, H.; Liu, Y.; Lercher, J. A. Influence of Hydronium Ions in Zeolites on Sorption. *Angew. Chem., Int. Ed.* **2019**, *58*, 3450−3455.

(50) Zhang, J.; Zhou, R.-J.; Chang, Q.-Y.; Sui, Z.-J.; Zhou, X.-G.; Chen, D.; Zhu, Y.-A. Tailoring catalytic properties of V2O3 to propane dehydrogenation through single-atom doping: A DFT study. *Catal. Today* **2021**, *368*, 46−57.

(51) Motagamwala, A. H.; Dumesic, J. A. Microkinetic Modeling: A Tool for Rational Catalyst Design. *Chem. Rev.* **2021**, *121*, 1049−1076.

(52) Baz, A.; Holewinski, A. Predicting macro-kinetic observables in electrocatalysis using the generalized degree of rate control. *J. Catal.* **2021**, *397*, 233−244.

(53) Mao, Z.; Campbell, C. T. Kinetic Isotope Effects: Interpretation and Prediction Using Degrees of Rate Control. *ACS Catal.* **2020**, *10*, 4181−4192.

(54) Campbell, C. T. The Degree of Rate Control: A Powerful Tool for Catalysis Research. *ACS Catal.* **2017**, *7*, 2770−2779.